Palacky University Olomouc
Faculty of Science

Department of Optics

Optimization of a polarization-entangled photon source

Diploma Thesis

Radim Hošák

2018

Palacky University Olomouc
Faculty of Science

Department of Optics

Optimization of a polarization-entangled photon source

Diploma Thesis

Author:	Radim Hošák
Study programme:	B1701 Physics
Field of study:	Optics and Optoelectronics
Form of study:	Full-time
Supervisor:	RNDr. Miroslav Ježek, Ph.D.
Thesis submitted on:	.....

Univerzita Palackého v Olomouci
Přírodovědecká fakulta

Katedra optiky

Optimalizace zdroje kvantově provázaných polarizačních stavů světla

Diplomová práce

Autor: Radim Hošák

Studijní program: B1701 Fyzika

Studijní obor: Optika a optoelektronika

Forma studia: Prezenční

Vedoucí: RNDr. Miroslav Ježek, Ph.D.

Práce odevzdána dne: .....

Abstract

An existing experimental setup for degenerate, non-collinear spontaneous parametric down conversion that generates correlated pairs of photons is optimized to achieve high-quality entanglement in the generated pairs. This Thesis is concerned with estimation and characterization of the generated quantum state, as well as with achieving as high entanglement as possible in the said state. Operation of the source in two regimes is demonstrated. With narrow-band spectral filters, state-of-the-art quality of entanglement can be achieved, with the concurrence of 99 % and approx. 16,000 coincidences per second. With wider-band filters, the rate of coincidences is just short of 100,000 per second, while the output state concurrence value is still very high, with a value of 96 %. In this Thesis, the techniques used to achieve such quality entanglement are described. Furthermore, a method of speeding up the quantum state tomography procedure is devised and applied.

Keywords

nonlinear optics, entanglement, spontaneous parametric down conversion

Acknowledgments

I would like to thank my parents, Jana and Vladimír, for their boundless love and material support, which they provided me with through five years of my university studies, and many years before that.

A huge thank you goes to my supervisor, Miroslav Ježek. Were it not for his patience with me, the Thesis could not be finished. He offered great advice which fuelled the work, and when things were not going smoothly, he supported me. I still have got a great deal to learn from him, and I can only hope that our cooperation will go on.

Everyone at the quantum optics lab helped me by creating a friendly and supportive environment. A special thank you goes to Martina Miková and Ivo Straka. They both helped me to get acquainted with lab equipment I could not make sense of on my own. I could always rely on Martina to listen to me, and on Ivo to show his programming prowess.

When I was working on this Thesis, I occasionally shared an office with my supervisor and three doctoral students—Jaromír Běhal, Josef Hloušek, and Robert Stárek. I would like to thank all of them for their patience with me. I am sorry for forgetting the keys and having to knock so often, and also for going in and out frequently while making trips to the department's kitchen to refill my mug. I was especially honored to be able to share the office with Robert Stárek, whose abilities and capacity I admire. It was a privilege to work with him on a paper which stemmed from this Thesis.

Lastly, I would like to thank Jan Bílek, a doctoral student who kick-started this project by assembling the basic form of the SPDC photon pair source setup, thus making it possible for me to focus my work on its characterization, and later, optimization.

Radim Hošák

Declaration

I hereby declare that I have written this Diploma Thesis—and performed all the presented research and experimental tasks—by myself, while being supervised by Miroslav Ježek. I also state that every resource used is properly cited. I agree with the Thesis being used for teaching purposes and being made available at the website of the Department of Optics.

Signed in Olomouc on ....

Radim Hošák

Contents

1 Introduction

1.1 Entanglement and its significance

This Thesis is focused on a source of photon pairs which are *entangled* in the polarization degree of freedom. Entanglement is a feature of composite physical systems that is of entirely quantum nature. The correlations shared by the entangled particles have no counterpart in the classical description of reality. Here, we will note the significance of the phenomenon of entanglement, and explore some of its possible practical applications.

The existence of entangled states has been predicted by quantum mechanics in its early days. In fact, it has been used as an argument against the theory in the famous Einstein's, Podolsky's and Rosen's *gedankenexperiment* from 1935 [1]. There, they argued that quantum mechanics, as it was, could not be a complete theory. On a hypothesized entangled state of two distant particles which shared correlations, or anti-correlations, in position and momentum, they tried to show that if the theory were to be realistic, one would have to be able to measure simultaneously, and with an arbitrary degree of precision, both the position and the momentum of the particles. This was in contradiction with the incompatibility of position and momentum postulated by the theory. Eventually, a theoretical approach to settle the debate was devised in the form of the *Bell's inequalities* [2], which were followed by propositions of their experimental verification, such as the *CHSH inequality* [3]. Violations of the inequalities have been observed [4, 5], and after a significant amount of research, we now have incontrovertible evidence in favor of quantum theory—the so-called *loophole-free* experimental violations of Bell's inequalities [6, 7]. In hindsight, we can identify the flaws in the reasoning of Einstein, Podolsky, and Rosen [8]. However, the argument, albeit flawed, is still of value, as it shows how drastically a physicist's way of thinking was forced to shift with the advent of the quantum theory.

The potential of quantum entanglement, however, reaches far beyond the historical matters. Over the years, many possible practical applications of entanglement have been proposed, and even demonstrated. For example, it has been shown that if two distant parties were to share two entangled particles, it will become possible to transfer the quantum state of another particle from one party to the other, using local operations and classical communication [9]. This phenomenon is known as *quantum teleportation*, and along with *entanglement swapping*, it has been demonstrated experimentally [10].

The particular properties of quantum states allow for applications in secure communication, giving rise to a field called *quantum cryptography*. Secret messages encoded with the *Vernam cipher* are virtually undecipherable, but they require that a so-called *one-time pad*—a single-use key that allows for encoding and decoding of the message—be generated and shared only between the authorized parties. It is the generation and transmission of the key between the two parties that benefits from the quantum approach called *quantum key distribution* (QKD). The virtue of QKD is that any breach of security of the transmission caused by an eavesdropper will inevitably lead to the destruction of the transmitted information, and this will be noticed by the communicating parties [11]. There have been proposals, and demonstrations of QKD protocols, such as BB84 [12, 13] and B92 [14, 15] that do not need entanglement and rely on non-orthogonal quantum states, and E91 [16, 17] which explicitly makes use of entanglement.

Apart from strengthening existing cryptography, entanglement can be in principle used to attack existing public-key cryptography [18] schemes that rely on the computational difficulty of *factoriza-*

tion of large integers, such as the RSA cryptosystem [19]. For a classical computer, there have been developed algorithms to find the prime factors of large numbers. However, there is no known factorization algorithm with polynomial (P) scaling of computation time with the size of the number to be factorized. On the other hand, there are such algorithms for a so-called *quantum computer* that relies on *quantum bits (qubits)* and *quantum gates*. One such example is *Shor's algorithm* [20]. Thanks to the features of the quantum world, such as superposition and entanglement [21], algorithms relying on quantum computers have the potential to outperform their classical counterparts.

Entangled systems can also be used to *simulate* [22] behaviour of other physical systems. This is advantageous especially if we don have enough control over them. Using a well-controlled entangled system, we can simulate quantum systems of sizes that would prove too much for a classical computer. For example, magnetic materials described by the *Ising model* can be simulated using a chain of quantum bits, where neighbouring qubits are entangled, to simulate ferromagnetic or diamagnetic behaviour. This has been achieved with trapped ions [23, 24, 25] and Rydberg atoms [26].

1.2 Entanglement sources

Entangled particles share correlations across multiple incompatible observables. This makes preparations of entangled states a non-trivial matter. We are, of course, able to prepare correlations in a particular observable rather easily, but correlations in other observables between the particles will not be present. Most techniques for generation of entangled states thus rely on physical processes where multiple particles are created simultaneously, or within a short time interval. Furthermore, we benefit from constraints laid upon the process, for example by conservation laws, to ensure that the generated particles share the desired correlations, or anti-correlations. Throughout the rest of this Thesis, we will consider only photons as the realization of quantum bits. Furthermore, we will limit ourselves to the discrete-variable scheme, with information encoded into the polarization degree of freedom.

The first experiments demonstrating the violation of Bell's inequalities relied on entangled photons generated in atomic cascades, such as the one in calcium [4, 5]. In an atomic cascade, an excited electronic state decays through a series of energy levels, emitting a photon during each de-excitation. The generated photons often vary in wavelength, as the energy levels are often not equidistant. There is, however, entanglement in polarization.

Shortly after the birth of nonlinear optics, processes such as the spontaneous parametric down-conversion (SPDC) in nonlinear optical crystals [27, 28] and, later on, four-wave mixing (FWM) in atomic vapours [29, 30, 31], were used to create entangled pairs of photons. Presently, SPDC-based entangled photon pair sources are the most widely used, as they are well-understood and reliable. To satisfy the *phase matching condition*, explained in Chapter 2, the SPDC sources either utilize *angular tuning* [27, 28], where the correct orientation of the pump and the generated photons with respect to the crystal ensures successful SPDC generation, or *temperature tuning* in conjunction with *periodic poling* [32, 33] of the crystal. The latter approach allows for greater length of the crystal, and thus a brighter source, while the first approach enables the use of a wide-band, pulse pump laser [34, 35].

Entanglement generation using nonlinear optics has also been demonstrated in optical fibers. The fiber-based sources often rely on FWM [36, 37, 38]. However, utilization of SPDC is also possible [39, 40]. The mechanical stress in the fibers induces asymmetry, enabling SPDC which would otherwise be impossible, as second-order nonlinear-optical processes are not observed in media with central symmetry [41].

Recently, there is an increasing interest in new light sources with intriguing properties and capabilities, such as quantum dots [42, 43], nitrogen-vacancy (NV) centers in diamond [44], photonic-band-gap and hybrid fibers [45], and on-chip photonic circuits [46], to name a few. However, further development is still required before entanglement sources based the mentioned techniques are widely adopted.

1.3 The aim of this Thesis

The goal of this Thesis is to take an existing SPDC-based experimental setup for photon pair generation and optimize it to achieve high quality of entanglement of the generated pairs, without sacrificing the rate of their generation. The resulting entanglement source differs in those already built in the Quantum Optics Lab Olomouc [47, 48], which brings along new challenges. A relatively new nonlinear material called BiBO [49] is used, with higher nonlinear coefficients than other commonly used crystals, such as BBO, KTP, or $LiNbO_3$ [50]. The source is designed while keeping in mind both continuous and pulsed [34, 35] laser to be used as pump. The non-collinear geometry of the output photons is also different from the already-built sources available at our lab.

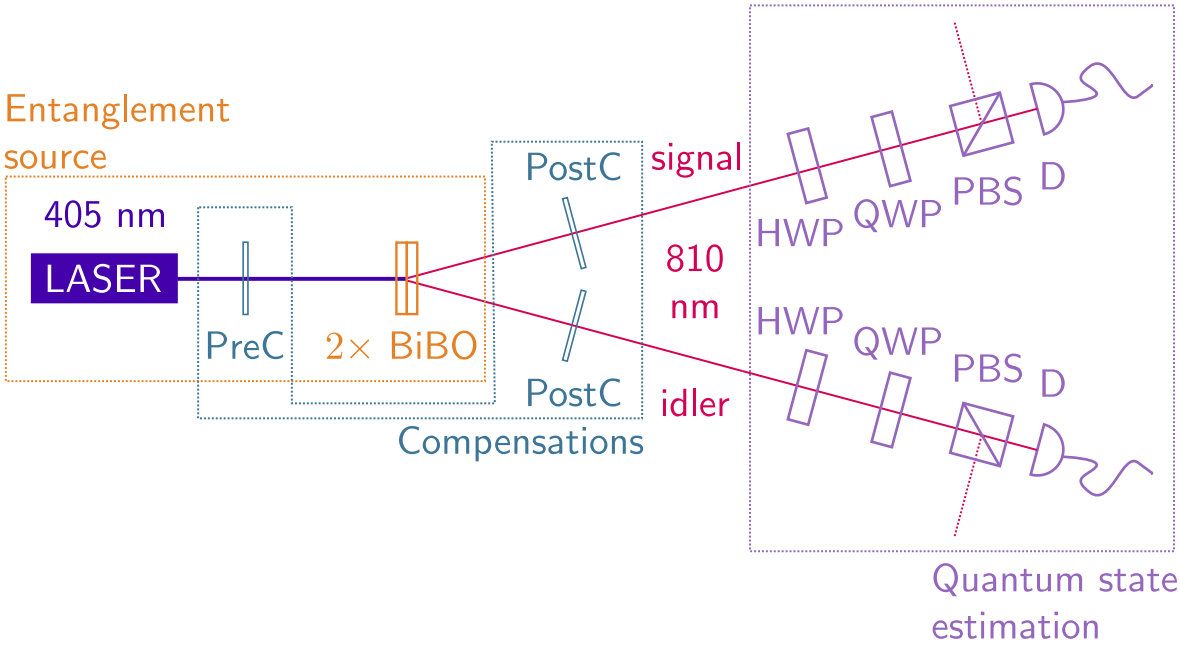

Figure 1.1: The schematic of the experimental setup for generation of entangled photon pairs, consisting of the source itself, quantum state estimation, and compensations of the source imperfections. The source consists of a strong laser pump and two BiBO crystals placed in series, generating the signal and idler beams which go off in different directions. Quantum state estimation utilizes half-wave plates (HWP), quarter-wave plates (QWP), and polarizing beam splitters (PBS). Detectors (D) are placed in one of the two output ports of each PBS. The compensation part relies on pre-compensating (PreC) and post-compensating (PostC) birefringent crystals which aim to eliminate the detrimental effect of the source imperfections on the entanglement of the generated photon pairs.

The schematic of the setup is shown in Figure 1.1. It is possible to divide the entire setup into three distinct parts—the *entanglement source*, *quantum state estimation*, and *compensations*. These parts correspond with the later chapters of the Thesis, and will be now described in more detail.

The central part of the entanglement source are two nonlinear BiBO crystals. They are positioned in a series, and their axes of birefringence are oriented so that they are mutually orthogonal [28]. The challenges surrounding the source itself come from the fact that BiBO is a biaxial crystal, which is uncommon among other presently used angularly tuned nonlinear crystals. In Chapter 2, the physical aspects of entanglement generation via the SPDC process, including phase matching, will be described.

To properly adjust and evaluate the entanglement source, full characterization of the quantum state is required. It is desirable that the tomographical procedure be automatized, and that it take the least amount of time, as it is a routine to be performed numerous times on a daily basis. The maximum-likelihood method will be used to infer the density matrix of the state, and entanglement criteria and measures will be applied to evaluate the presence and quality of entanglement, respectively. This is the focus of Chapter 3.

Entanglement sources based on angularly tuned birefringent crystals feature some imperfections in the generated photons, which lead to *which-crystal information* and the overall degradation of entanglement. Most notable example is the effect called *walk-off*. To compensate such imperfections, birefringent compensation crystals need to be used, both before and after the BiBO crystals. To evaluate the effect of compensations on the generated quantum state, mainly on its quality of entanglement, we will make use of the full state characterization techniques. In Chapter 4 we will discuss walk-off and see how the quality of entanglement in the generated photon pairs depends on the presence and orientation of the compensating elements. Eventually, we will arrive at a quantum state with nearly perfect entanglement.

Each of the chapters described above will start with a presentation of the necessary theoretical aspects and then discuss the matters related to the experimental realization on the SPDC entanglement source. The concluding Chapter 5 serves to provide a concise overview of the resulting characteristics of the entanglement source, and hints at some possible future improvements to the setup, as well as its applications in other experimental projects.

2 The SPDC-based entanglement source

2.1 Introduction to SPDC

Spontaneous parametric down conversion is a non-resonant nonlinear-optical process. Optical nonlinearity arises from the nonlinear dependence of the polarization vector $\mathbf{P}$ on the applied electric field $\mathbf{E}$ in certain media. This dependence is given by the nonlinear electric susceptibility χ of the given medium. SPDC is second-order process, which means that it relies on the quadratic part of the nonlinear susceptibility, denoted $\chi^{(2)}$ [41].

The basic concept of nonlinear-optical processes is that if strong enough, the applied electric field $\mathbf{E}$ can generate a response in the form of $\mathbf{P}$, which oscillates not only with the same frequency as $\mathbf{E}$, but also at different frequencies. This in turn gives rise to respective outcoming optical fields. In the case of SPDC, the applied field E_p, called the *pump* generates outcoming field with two chromatic components $E_\mathrm{s}, E_\mathrm{i}$ called the *signal* and the *idler*, respectively. The energy conservation law implies strong anti-correlations in the frequencies of signal and idler. The wave vector conservation law (the *phase-matching condition*), if satisfied using birefringent media, can lead to entanglement in polarization.

In the most basic form, SPDC can be understood as a photon scattering process where one pump photon, with frequency ω_p and wave vector $\mathbf{k}_\mathrm{p}$ is absorbed in a medium, followed by the emission of two photons, signal and idler, with frequencies and wave vectors $\omega_\mathrm{s}, \mathbf{k}_\mathrm{s}$ and $\omega_\mathrm{i}, \mathbf{k}_\mathrm{i}$, respectively. This is portrayed using a schematic in Figure 2.1a.

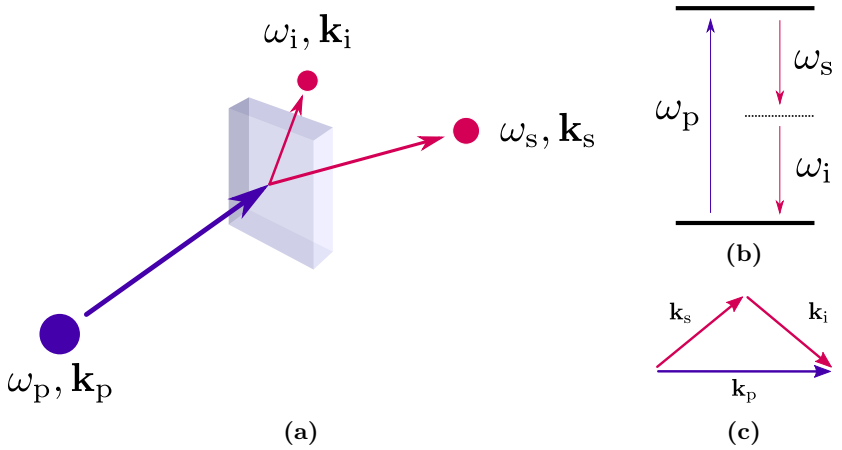

Figure 2.1: A phenomenological description of the SPDC process. A schematic (a) shows SPDC as a photon scattering process. The energy-level diagram (b) visualizes the energy conservation law (2.1). The phase-matching condition (2.3) is shown in (c).

Two conditions must be met in order to observe this process. The energy conservation law

$$\hbar\omega_\mathrm{p} = \hbar\omega_\mathrm{s} + \hbar\omega_\mathrm{i} \tag{2.1}$$

states that the energy of the two generated photons must match the energy of the absorbed one. By dividing both sides of (2.1) by $\hbar$, we arrive at

$$\omega_\mathrm{p} = \omega_\mathrm{s} + \omega_\mathrm{i}. \tag{2.2}$$

Furthermore, momentum must be conserved:

$$\hbar\mathbf{k}_\mathrm{p} = \hbar\mathbf{k}_\mathrm{s} + \hbar\mathbf{k}_\mathrm{i}. \tag{2.3}$$

Again, upon dividing both sides of (2.3) by $\hbar$ we obtain

$$\mathbf{k}_\mathrm{p} = \mathbf{k}_\mathrm{s} + \mathbf{k}_\mathrm{i}, \tag{2.4}$$

which is known as the *phase-matching condition* [41]. We can write (2.4) as

$$\Delta\mathbf{k} = \mathbf{0}, \tag{2.5}$$

where we define the *phase mismatch*:

$$\Delta\mathbf{k} = \mathbf{k}_\mathrm{p} - \mathbf{k}_\mathrm{s} - \mathbf{k}_\mathrm{i}. \tag{2.6}$$

2.2 Classical description of SPDC: coupled wave equations

If we assume that two monochromatic components $\mathbf{E}_3$, $\mathbf{E}_2$ of the electric field vector $\mathbf{E}$ are present in the medium, and that they oscillate at angular frequencies and with wave vectors ω_3, $\mathbf{k}_3$, and ω_2, $\mathbf{k}_2$ respectively, $\omega_3 > \omega_2$, then the second-order contribution $\mathbf{P}^{(2)}$ to the nonlinear polarization vector $\mathbf{P}$ oscillating at frequency $\omega_1 = \omega_3 - \omega_2$ and with wave vector $\mathbf{k}_1$ is given as

$$\mathbf{P}^{(2)} = \varepsilon_0 \chi^{(2)} \mathbf{E}_3 \mathbf{E}_2^* e^{-i(\omega_3 - \omega_2)} e^{-i\Delta\mathrm{k}}, \tag{2.7}$$

This part of the second-order polarization vector $\mathbf{P}^{(2)}$ is a source of the electric vector $\mathbf{E}_1$ oscillating at angular frequency ω_1, as can be seen from the wave equation for a nonlinear medium:

$$\nabla^2 \mathbf{E}_1 - \frac{n^2}{c^2}\frac{\partial^2 \mathbf{E}_1}{\partial t^2} = \mu_0 \frac{\partial^2 \mathbf{P}^{(2)}}{\partial t^2}. \tag{2.8}$$

We now apply this to the case of SPDC. We identify the field $\mathbf{E}_3$ with the pump, and the fields $\mathbf{E}_1, \mathbf{E}_2$ with signal and idler, respectively. We are interested in frequency-degenerate SPDC, meaning that the down-converted fields $\mathbf{E}_1$ and $\mathbf{E}_2$ both oscillate at the same frequency $\omega_1 = \omega_2$. By employing the slowly-varying envelope approximation, it is possible to arrive at the following *coupled wave equations* for the amplitudes A_1, A_2 of the generated down-converted electric fields:

$$\frac{\mathrm{d}A_1}{\mathrm{d}z} = \frac{i\omega_1^2 \chi^{(2)}}{k_1 c^2} A_3 A_2^* \mathrm{e}^{i\Delta k z}, \tag{2.9}$$

$$\frac{\mathrm{d}A_2}{\mathrm{d}z} = \frac{i\omega_2^2 \chi^{(2)}}{k_2 c^2} A_3 A_1^* \mathrm{e}^{i\Delta k z}. \tag{2.10}$$

The solutions to the Equations (2.9) and (2.10) for the case of perfect phase matching $\Delta\mathbf{k} = \mathbf{0}$ are the hyperbolic functions sinh and cosh, leading to increase in the amplitude of the down-converted fields as the pump propagates through the nonlinear medium.

Note that the description above assumes that some, however small, amount of one of the generated fields $\mathrm{E}_1, \mathrm{E}_2$ is already present. However, SPDC is a *spontaneous* process, meaning that the presence of the fields E_1 and E_2 is not necessary for the process to start. To account for spontaneity of SPDC, quantum-mechanical treatment would be required.

2.3 Phase matching in a biaxial birefringent crystal

Now we focus on the phase-matching condition itself. We are interested in the case of zero phase mismatch $\Delta\mathbf{k} = \mathbf{0}$ for which the process is most effective. Upon separating the wave vectors into their scalar components

$$\mathbf{k}_i = \sum_{j=1}^{3} \hat{e}_j k_i^j, \qquad k_i^j = \frac{\omega_i}{c} n_i \cos\alpha_i^j, \qquad i = 1, 2, 3, \tag{2.11}$$

where $\hat{e}_j$ are the three canonical base vectors and $\cos\alpha_i^j$ are the directional cosines of the i^{th} wave, we can see that the refractive indices n_i play a role in the phase matching condition. As real optical media are dispersive, the indices n_i are frequency-dependent. Using a birefringent medium additionally makes the refractive indices n_i angularly dependent. This opens up the possibility of finding for the three interacting waves a set of direction of propagation such that they each experience the correct refractive index as to satisfy the phase-matching

The task of finding the correct angles of propagation of the three waves with respect to the optical axes of the crystal usually involves solving a system of equations. In these equations, both the angular and frequency dependence of the refractive index are explicitly present, the latter often being approximated by the Sellmeier relations.

2.4 The Kwiat's Type-I entanglement source

With the possibility of generating pairs of photons in an angularly-tuned phase-matched birefringent crystal, we proceed to show how the SPDC process can be applied to achieve entanglement in the generated pairs. For Type-I phase matching, a commonly used geometry is the one shown in Figure 2.2. Two nonlinear crystals are used, and their axes of birefringence are perpendicular to each other. Furthermore, the pump beam is diagonally polarized with respect to the axes.

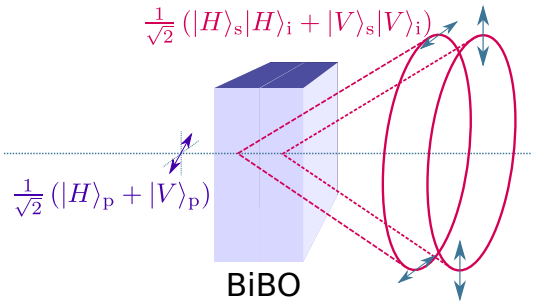

Figure 2.2: A schematic of the Kwiat's Type-I entanglement source. Two BiBO crystals are placed in series, with orthogonal birefringent axes. Diagonally polarized pump beam causes SPDC in both the crystals. Signal and idler are generated in two overlapping cones.

If the first crystal was oriented in such a manner that a vertically polarized pump generates via SPDC pairs of horizontally polarized photons:

$$|V\rangle_p \to |H\rangle_s|H\rangle_i \tag{2.12}$$

then the second crystal, with optical axis perpendicular to the axis of the first crystal, will generate vertically polarized photons when pumped horizontally

$$|H\rangle_p \to |V\rangle_s|V\rangle_i \tag{2.13}$$

and since the pump is diagonal, both of these processes will occur at once:

$$\frac{1}{\sqrt{2}}\left(|H\rangle_{\mathrm{p}}+|V\rangle_{\mathrm{p}}\right)\rightarrow\frac{1}{\sqrt{2}}\left(|H\rangle_{\mathrm{s}}|H\rangle_{\mathrm{i}}+|V\rangle_{\mathrm{s}}|V\rangle_{\mathrm{i}}\right) \tag{2.14}$$

The SPDC process in question is non-collinear, meaning that the pump and the generated photon pairs do not propagate in a single common direction. Effectively, we observe that the photon pairs generated from the two SPDC crystals fly off in two separate cones, as shown in Figure 2.2.

Now we describe the experimental setup, shown in Figure 2.3, that is used throughout the rest of this Thesis. We use a fiber-coupled 405 nm laser (`Toptica iBEAM-SMART-PT-405`) as a pump. The power of the laser just before the SPDC crystals is approximately 43 mW, and the laser is not frequency-stabilized. The pump passes through a half-wave plate $\mathtt{HWP_p}$ which allows us to rotate its plane of linear polarization. After being focused by a lens $\mathtt{L_p}$, the pump is incident on the two BiBO crystals, both 0.5 mm thick, and the rest of the pump beam that passes through unaffected is stopped. The signal and idler SPDC photons—visualized by red and orange lines, respectively, in Figure 2.3—are generated in cones with an opening angle of 3 ° and are deflected using a split prism. In both the signal and the idler arm of the setup, the generated photons are focused by lenses $\mathtt{L_s}, \mathtt{L_i}$, steered through a series of irises $\mathtt{I_s}, \mathtt{I_i}$ in order to facilitate maintenance of the source geometry, and finally coupled to single-mode fibers, shown as thin curved lines in Figure 2.3. Before coupling to fibers, the photons pass through narrow-band interference-based frequency filters $\mathtt{IF_s}, \mathtt{IF_i}$ centered about 810 nm.

An important element of the fiber-part of the setup are the polarization controllers $\mathtt{PC_s}, \mathtt{PC_i}$ they play a role once the signal and idler photons leave the single-mode fibers and enter the quantum state estimation part of the setup, described in more detail in Chapter 3. This part of the experiment consists of half-wave plates $\mathtt{HWP_s}, \mathtt{HWP_i}$, quarter-wave plates $\mathtt{QWP_s}, \mathtt{QWP_i}$, polarizing beam splitters $\mathtt{PBS_s}, \mathtt{PBS_i}$. After passing these components, the photons are coupled into multi-mode fibers, denoted by thick curved lines in Figure 2.3. Before that, however, cut-off frequency filters $\mathtt{CF_s}, \mathtt{CF_i}$ are used to reduce the amount of stray light coupled into the multi-mode fibers along with the desired SPDC-generated photon pairs. The fibers are connected to single photon avalanche detectors, and the signal from them is in turn fed into coincidence logic and a multi-channel counter.

There are some components that were not so far listed. They are the pre-compensator `PreC` and the post-compensators $\mathtt{PostC_s}, \mathtt{PostC_i}$. They aim to eliminate the effect of the entanglement-degrading mechanisms inherently present in the described scheme. Compensations will be studied in Chapter 4.

Figure 2.3: The experimental setup. Pump, signal, and idler beams are visualized as blue, red, and orange lines, respectively. Single-mode fibers are denoted by thin curved lines, and multi-mode fibers by thick curved lines. **CF**: cut-off filter, **HWP**: half-wave plate, **I**: iris, **IF**: interference filter, **L**: lens, **M**: mirror, **PBS**: polarizing beam splitter, **PC**: polarization controller, **PostC**: post-compensator, **PreC**: pre-compensator, **QWP**: quarter-wave plate. Lower indices indicate the **p**ump, **s**ignal, and **i**dler parts of the setup.

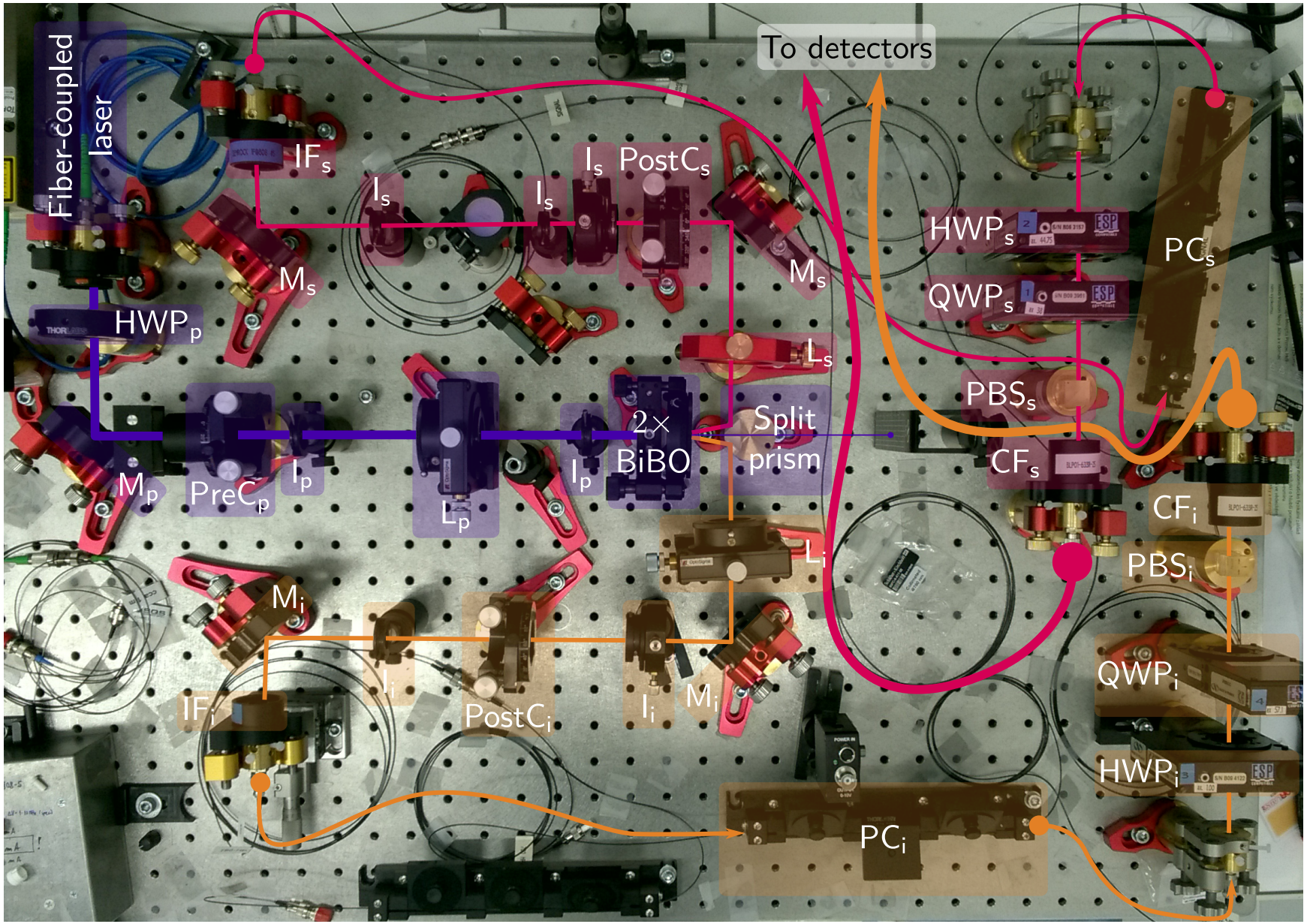

3 Output state tomography

3.1 Introduction to quantum state tomography

Estimating an unknown state of a single-qubit system by means of quantum state tomography requires projecting the state onto a certain set of states. Usually, the tomography consists of projection onto the six states: the horizontal (H), vertical (V), diagonal (D), anti-diagonal (A), right-circular (R), and left-circular (L), which form three mutually unbiased bases [51]. The measurements are often realized using a sequence of a half-wave plate (HWP), a quarter-wave plate (QWP), and a polarizing beamsplitter (PBS), shown in Figure 3.1a. Without the waveplates, the H state can be measured behind the PBS. Different projections can be measured using the waveplates, more specifically by adjusting the angles ϕ and θ of the optical axes of the HWP and QWP, respectively, with respect to the plane of horizontal polarization. The waveplate angles corresponding to the six projections, valid for the order of waveplates shown in Figure 3.1a are given in Table 3.1.

symbol	**state**	**HWP** (ϕ)	**QWP** (θ)
H	horizontal	0	0
V	vertical	45	0
D	diagonal	22.5	0
A	anti-diagonal	-22.5	0
R	right-circular	0	45
L	left-circular	0	-45

Table 3.1: The six one-qubit polarization projections and the corresponding waveplate angles.

For a two-qubit system, it is not enough to perform the one-qubit procedure for each individual qubit. Whereas the single-qubit density matrix is given by $4 - 1 = 3$ independent parameters, the two-qubit density matrix requires $4^2 - 1 = 15$ parameters [51]. We can see that we would not obtain enough data to properly reconstruct the density matrix. If we denote $\mu_1 = |H\rangle\langle H|, \mu_2 = |V\rangle\langle V|, \ldots$ the operators describing our 6 polarization projection measurement, we perform the multi-qubit tomography by the means of operators

$$\mu_{ij} \equiv \mu_i \otimes \mu_j, \qquad i = 1, 2, \ldots, 6, \quad j = 1, 2, \ldots, 6. \tag{3.1}$$

The number of performed measurement then rises from 6 to 36. Furthermore, the technique of measurement changes as well. In single-qubit state tomography, our measurement results are the detected intensities of—or, in case of weak signal, detector counts caused by—the optical signal after the PBS. With multi-qubit tomography, we must evaluate the *coincidence rate* rather than the *single detections*—individual signals from all the involved detectors. This is often done by feeding the output of the detectors into electronic circuitry, which we will further call *coincidence logic* (see Figure 3.1b). Here, the signals from both detectors first pass through a *discriminator*, which takes pulses with amplitude that exceeds a certain threshold and outputs rectangular pulses with a given length in their place. The resulting signal from the two discriminators then enters the coincidence unit itself. If two

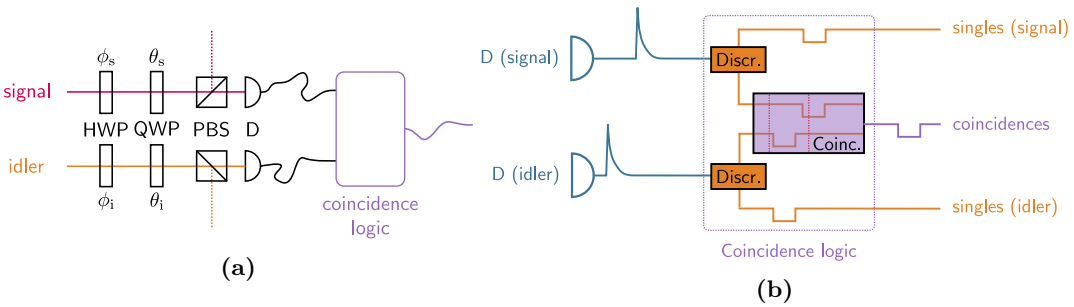

Figure 3.1: The used polarization tomography scheme (a). The signal and idler photons from the output of the SPDC source pass through a half-wave plate (HWP), a quarter-wave plate (QWP) and a polarizing beam splitter (PBS). The fraction of intensity detected by the detector (D) then corresponds to the projection of the output state into one of the 36 tomographical projections. The coincidence logic (b) consists of discriminators (Discr.) which produce negative NIM pulses, and a coincidence unit (Coinc.), which outputs a pulse when the two pulses arrive within a certain time window, shown with red dotted lines.

pulses arrive within a certain time window, the coincidence unit outputs a pulse. These pulses are then counted using a multi-channel counter. Single clicks are counted as well, and are used during source adjustment and maintenance.

3.2 Minimal-time tomography strategy

For each polarization projection measurement, the waveplates must be oriented at specific angles. When we wish to move from one projection to another, at least one of the waveplates needs to be readjusted. This is done using motorized rotation mounts which are computer-controlled via serial interface. The readjustment of the waveplates takes different amounts of time, depending on the angle travelled and the type of the rotation mount. This opens up the possibility to optimize the order of projection measurements with respect to the total time spent on reorienting the waveplates between measurements.

For one-qubit tomography, it is feasible to find the projection measurement order that minimizes the total time spent on reorienting the waveplates by a simple brute-force algorithm. Such an algorithm would go through all permutations of the HVDARL sequence and add up the total time that is spent on all the transitions between polarization projection measurements. After all possible permutations have been checked, the algorithm would return the one that minimized the total time spent on the transitions. However, this approach cannot be used for larger systems. The total number of all possible orderings of the measurements is $6^n!$ where n is the number of qubits that the system consists of. For the one-qubit case, this gives $6! = 720$ permutations to check, but for a two-qubit system, there are $6^2! \approx 10^{41}$ possibilities. Thus, to optimize the polarization projection order, we regarded the task as an instance of the travelling salesman problem (TSP) [52] and solved it using the state-of-the-art branch and bound algorithms [52, 53].

The TSP is a well-known problem of graph theory. We will use the common graph-theoretical terminology, and proceed to call the set of projection measurements a graph. The individual measurements will be known as nodes of the graph. Between each two nodes, there is an edge, corresponding to a transition from the first to the second node. The edges are weighted, which means that different transitions take a different amount of time. The graph is visualized for the case of one-qubit tomography in Figure 3.2a.

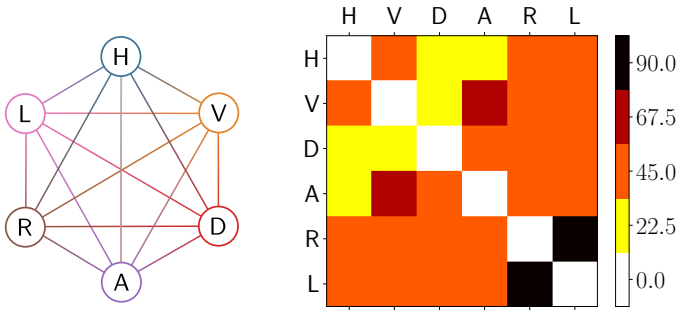

(a) (b)

Figure 3.2: A graph representation of one-qubit tomography (a). The graph nodes correspond to the six projection measurements. All graph edges are shown as lines. The graph edge weights are represented by the adjacency matrix (b). The matrix elements correspond to the largest angle that any waveplate has to be rotated by during a given transition. The most demanding transitions, represented by black, are those between the R and L polarization states.

The durations of transitions between the projection measurements depend heavily on the particular type of rotation mount used. However, if we consider the situation where all the rotation mounts rotate equally fast, with uniform angular velocity throughout each and every possible transition between the tomographical projections, we can formulate the TSP in terms of angle travelled, instead of time spent on readjusting the waveplates [54, 55]. This approach makes the formulation clearer, as the edge weights can be checked by comparison with Table 3.1. Furthermore, the results obtained from the optimization are device-independent, as long as the real rotation mounts satisfy the initial assumption of uniform angular velocity. As multiple waveplates may need to be readjusted during a single transition, we take the maximal angle—absolute valued—travelled by any waveplate during the transition, and consider that the weight of the corresponding graph edge.

With a set of graph nodes, and the values of all graph edge weights, we have all the information needed to specify the instance of a TSP. This data is commonly organized into an *adjacency matrix* [52, 56]. Its elements C_{ij} are the weights of the edges $i \to j$, or the transitions from projection measurement i to measurement j. The diagonal elements of this matrix are zero, and the matrix is symmetrical for our case. The adjacency matrix for one-qubit tomography, corresponding to the experimental setup shown in Figure 3.1a and the waveplate angles from Table 3.1 is shown in Figure 3.2b.

To quantify the reduction in time achieved using a TSP-optimized measurement sequence, we use the *speedup factor*

$$s = \frac{\tau_{\text{conv}}}{\tau_{\text{TSP}}}, \tag{3.2}$$

where τ_{TSP} is the total transition duration for the TSP-optimized measurement order, and τ_{conv} is the total duration for the conventional order, by which we mean the order in which the six projections were introduced: H, V, D, A, R, and L. Both τ_{TSP} and τ_{conv} include the transition from the final projection to the first one, completing a cycle. τ_{conv} can be computed from the adjacency matrix as

$$\left(\sum_{i=1}^{5} C_{i,i+1}\right) + C_{6,1}. \tag{3.3}$$

For the example of one-qubit tomography, we use (3.3) to arrive at $\tau_{\text{conv}} = 292.5\,°$, and the TSP

conv	H		V		D		A		R		L		H
$\tau_{\text{conv}} = 292.5\,°$		45		22.5		45		45		90		45	
TSP	H		L		A		R		V		D		H
$\tau_{\text{TSP}} = 225\,°$		45		45		45		45		22.5		22.5	

Table 3.2: The conventional and TSP-optimized sequence for the example case of one-qubit tomography. The order of projection measurements is shown for both, along with the maximal angle travelled by any waveplate during individual transitions, including the transition between the final and the initial measurement, completing a cycle.

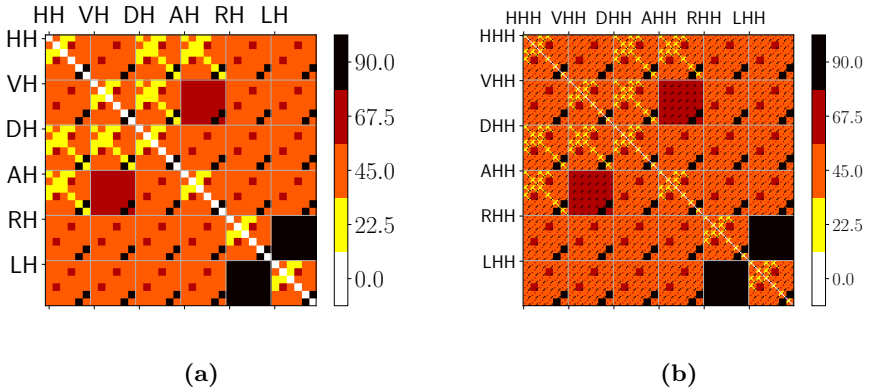

(a) **(b)**

Figure 3.3: The adjacency matrices for the two-qubit (a) and three-qubit (b) quantum state tomography TSPs. Curiously, the matrices resemble fractal-like objects.

algorithm finds an optimal sequence with $\tau_{\text{TSP}} = 225\,°$. The speedup factor computed using (3.2) is then $s = 1.3$. Working with transition angles instead of temporal durations has no effect on the end result, provided that all waveplates rotate with uniform angular speed. This sequence is listed in Table 3.2.

In our scenario, we concern ourselves with tomography of a two-qubit system. This means that our TSP graph has 36 nodes. Again, by using the assumption of a uniform angular velocity for all the waveplate mounts, we can arrive at an angularly specified adjacency matrix shown in Figure 3.3a. In order to gain an insight into how the speedup factor scales with the size of a quantum system, we performed the TSP optimization of an up to five-qubit system [54]. The resulting speedup factors are plotted in Figure 3.4. With an adjacency matrix of size 7776×7776, we were not able to solve the six-qubit tomography TSP on a consumer-grade laptop. Exact solution of the TSP for even large systems, however, will quickly become impossible for any modern computer. This is due to the non-polynomial (NP) scaling of the TSP. Upon comparing the two-qubit TSP adjacency matrix from Figure 3.3a with the tree-qubit matrix in Figure 3.3b, it is interesting to note the apparent self-similarity present in the adjacency matrices for n-qubit tomography TSP with angular specification of the graph weights. This might show that the problems of optimizing such tomographical tasks form a distinct subset of the general TSP problem. This fact may have some interesting implications. Their rigorous study is, however, beyond the scope of this Thesis.

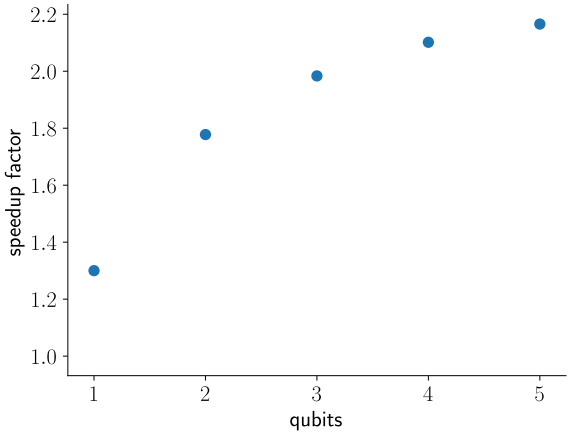

Figure 3.4: The speedup factor for increasingly larger systems of qubits. We see an increasing trend, and the speedup factor nearly reaches a value of 2 for a three-qubit system already.

3.3 Tomography optimization for the SPDC source

In our setup, the angular specification of the tomography TSP cannot be used, as three of the waveplates are in slow mounts, while a fourth one—a quarter-wave plate in the idler branch—is in a fast mount. We thus rely on temporal specification. The times of all the possible rotations the waveplates might undergo during the tomographical procedure were obtained using serial interface communication with the mounts. From this information we assembled the adjacency matrix, which can be seen in Figure 3.5, where we took the liberty to divide the data into second-long bins. However, when the TSP was being solved, the accurate values were used.

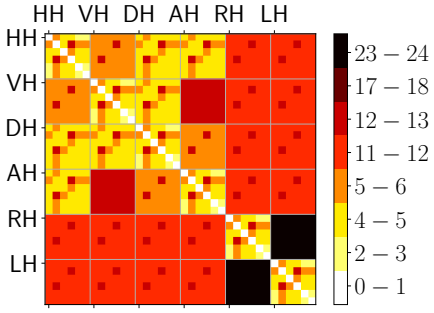

Figure 3.5: The adjacency matrix for our real-world two-qubit tomography TSP with three slower rotation mounts and one fast mount used for a QWP. For clearer presentation, the matrix elements have been divided into second-long bins.

We use (3.3) to obtain $\tau_{\text{conv}} = 352\,\text{s}$. The TSP algorithm found an optimal measurement sequence with $\tau_{\text{TSP}} = 206\,\text{s}$. The speedup factor is then $s = 1.71$. The TSP-optimized sequence of measurements is shown in Table 3.3.

HH	HA	AH	AD	AV	AA	RR	RL	RD	RH	RA	RV
AL	AR	HL	HR	DR	DL	VL	VR	LR	LL	LA	LV
LD	LH	VV	VD	VH	VA	DD	DV	DA	DH	HV	HD

Table 3.3: The TSP-optimized sequence of 36 measurements for two-qubit state tomography in our setup with three slow rotation mounts and one fast mount. The sequence is to be read left-to-right, top-to-bottom.

3.4 Maximum-likelihood quantum state estimation

Maximum-likelihood estimation (MaxLik) [57, 58] is a method of statistical inference that tries to answer the following question: "What physical density matrix ρ is the most likely to have generated the measured data?" This approach sets it apart from the *direct inversion* method. The word "physical" refers to the fact that the obtained density matrix ρ should be Hermitian, positive semi-definite, and have a trace equal to unity.

Let our measurement apparatus be described by a positive operator valued measure (POVM)

$$\{\Pi_i\}_{i=1}^{N}, \qquad \sum_{i=1}^{N} \Pi_i = I, \tag{3.4}$$

where Pi_i is the POVM operator corresponding to the i^{th} outcome of the measurement, N is the number of possible measurement outcomes, and I is the identity operator. Then, for a quantum state described by a density matrix ρ, the outcome i of the measurement has the probability [57]

$$p_i^{(\rho)} = \mathrm{Tr}\left(\rho\Pi_i\right). \tag{3.5}$$

If those probabilities were known, an inversion of the linear relation (3.5) would yield the density matrix ρ [59] In reality, however, the probabilities are not known. Instead, we measure the relative frequencies of outcomes $\{f_i\}_{i=1}^{N}$. These are not equivalent to the probabilities $\{p_i\}$, and so the inversion cannot guarantee a correct result.

Instead of the direct inversion of (3.5) we seek the density matrix ρ that maximizes the likelihood functional [59]

$$\mathcal{L}\left(\rho\right) = \prod_{i=1}^{N} \langle y_i|\rho|y_i\rangle^{f_i}, \tag{3.6}$$

where $|y_i\rangle$ is the pure state corresponding to outcome i of the measurement apparatus. From here, we can proceed formally and solve the corresponding Lagrange equation, or we can use the iterative algorithm described below.

The estimation starts with an initial density matrix ρ_0. We choose it to be a 4×4 unit matrix, normalized such that $\mathrm{Tr}\left(\rho_0\right) = 1$. Next, Equation (3.5) is used to compute the probabilities of the 36 polarization projection measurements for the state described by ρ_0. In our case, the POVM operators Π_i are the outer products $|HH\rangle\langle HH|$, $|HV\rangle\langle HV|$, and so on. With the newly obtained probabilities $p_i^{(\rho_0)}$ we can proceed to compute the following matrix:

$$R = \sum_{i=1}^{36} \frac{f_i \Pi_i}{p_i^{(\rho_0)}}. \tag{3.7}$$

Finally, we obtain a new density matrix ρ_1:

$$\rho_1 = R\rho_0 R. \tag{3.8}$$

This procedure is repeated a numerous times: for ρ_n, new probabilities $p_i^{(\rho_n)}$ are obtained, the matrix R is computed, finally resulting in a new matrix ρ_{n+1}. We chose to perform 1,000 iterations of the MaxLik algorithm for each state we estimated. However, even fewer were needed, as the estimation converges rather quickly.

3.5 Quantum state characterization

With the estimated density matrix ρ of the generated photon pair state, we can proceed to answer the following questions: Does ρ belong to a pure state, or a mixed state? Is the quantum state entangled? And if so, how well entangled is it? To answer the first question, we evaluate the *purity* of the density matrix, the second question is answered by *entanglement criteria*, and *entanglement measures* answer the last one.

The purity of a quantum state is defined as

$$\gamma(\rho) = \mathrm{Tr}\left(\rho^2\right) \tag{3.9}$$

A perfectly pure state has a purity of one. On the other hand, a perfect mixture of states has a purity equal to $1/d$, where d is the dimension of the Hilbert space in question.

Density matrices of non-entangled quantum systems have one property that distinguishes them from their entangled counterparts: *separability*. Suppose that the non-entangled system in question consists of two particles with density matrices ρ'_A and ρ''_A, respectively. Then the separability of the density matrix ρ of the bipartite system means that ρ can be expressed as a sum of direct products:

$$\rho = \sum_A w_A \rho'_A \otimes \rho''_A, \tag{3.10}$$

or, with explicitly denoting the matrix elements:

$$\rho_{m\mu,n\nu} = \sum_A w_A \left(\rho'_A\right)_{mn} \left(\rho''_A\right)_{\mu\nu} \tag{3.11}$$

On the other hand, if ρ were not separable, it would mean that the quantum state in question is entangled. However, a direct verification of separability by finding the sum (3.10) is tedious. Instead, the *positive partial transpose criterion* is commonly used. First, a partial transpose of the density matrix ρ is found by transposing the matrix indices of ρ that belong to one of the subsystems:

$$\sigma_{m\mu,n\nu} \equiv \rho_{n\mu,m\nu}. \tag{3.12}$$

The positive partial transpose criterion states that if the partial transpose σ has negative eigenvalues, then the density matrix ρ belongs to a non-separable state. In general, it is a necessary condition for ρ. However, for density matrices of subsystems of dimension 2×2 it is also a sufficient condition.

To quantify the quality of entanglement of the generated pairs, and also in order to evaluate the effect of pre- and post-compensations, entanglement measures are needed. One of the many commonly used measures is *concurrence*. For a quantum state described by the density matrix ρ, concurrence is defined as

$$C(\rho) \equiv \max\left\{0, \lambda_1 - \lambda_2 - \lambda_3 - \lambda_4\right\}, \tag{3.13}$$

where λ_i are, in decreasing order, the eigenvalues of the matrix

$$R \equiv \sqrt{\sqrt{\rho}\tilde{\rho}\sqrt{\rho}}. \tag{3.14}$$

The matrix $\tilde{\rho}$ is obtained in the following fashion:

$$\tilde{\rho} \equiv (\sigma_y \otimes \sigma_y)\, \rho^* \,(\sigma_y \otimes \sigma_y)\,, \tag{3.15}$$

where the star denotes complex conjugation and σ_y is the 2×2 Pauli matrix

$$\sigma_y \equiv \begin{pmatrix} 0 & -i \\ i & 0 \end{pmatrix}. \tag{3.16}$$

The value of concurrence ranges from 0 to 1, reaching 1 for the maximally entangled states, and 0 for completely non-entangled states.

From concurrence other entanglement measures can be readily computed. Firstly, the multipartite entanglement measure *tangle* is in the case of a bipartite state simply reduced to the square of concurrence:

$$T\,(\rho) \equiv [C\,(\rho)]^2\,. \tag{3.17}$$

Another commonly used entanglement measure is *entanglement of formation*. It is a convex function of concurrence, and is defined as

$$E\,(\rho) = \mathcal{E}\,[C\,(\rho)] \tag{3.18}$$

with

$$\mathcal{E}\,(C) \equiv -\frac{1+\sqrt{1-C^2}}{2}\log_2\frac{1+\sqrt{1-C^2}}{2} - \frac{1-\sqrt{1-C^2}}{2}\log_2\frac{1-\sqrt{1-C^2}}{2}. \tag{3.19}$$

The entanglement measures mentioned above share one common trait: invariance under unitary transformations. More specifically, a density matrix $\tilde{\rho}$, obtained from ρ by a unitary transformation U

$$\tilde{\rho} = U^\dagger \rho\, U, \tag{3.20}$$

has the same concurrence, tangle, and entanglement of formation as the unmodified density matrix ρ. This invariance is not the case for another quantifier of entanglement: Bell state fidelity. If we take it as our goal to generate one of the maximally entangled Bell states $|\psi_{\mathrm{B}}\rangle$, it is reasonable to seek to maximize the overlap between the density matrix ρ of our generated bipartite state, and $|\psi_{\mathrm{B}}\rangle$. This is the Bell state fidelity

$$\mathcal{F}^{(\psi_{\mathrm{B}})} \equiv \mathrm{Tr}\langle\psi_{\mathrm{B}}|\rho|\psi_{\mathrm{B}}\rangle. \tag{3.21}$$

If the density matrix ρ has been modified by an unwanted unitary transformation U, however, the fidelity will change its value. To mitigate this, we can try to compensate U by physically introducing another transformation $\tilde{U}$, which we have some control over, and try to achieve $\tilde{U} = U^\dagger$. Unfortunately, this might not be always possible. If we still wish to evaluate the Bell state fidelity, we could introduce $\tilde{U}$ numerically, on the density matrix obtained via the MaxLik algorithm. When we use this approach in the Thesis, we will always explicitly state so.

3.6 Error propagation

During each polarization projection measurement, we count the number of coincidences registered during a certain time interval. If we were to perform this measurement repeatedly, we would observe some fluctuations of the coincidence counts. This is due to the fact that we are merely sampling the

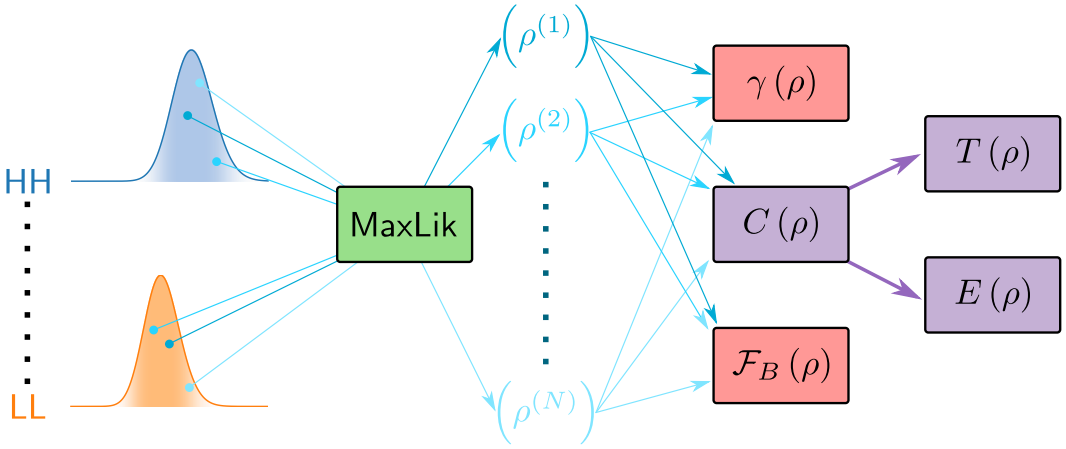

Figure 3.6: A description of the Monte Carlo technique. The coincidence counts for the 36 projections are sampled N times from Poissonian distributions with means equal to the respective measured coincidence counts. These distributions are shown schematically for the HH and LL projections. Each set of the N sets of 36 coincidence count samples is fed to the MaxLik algorithm, resulting in N density matrix estimates, from which the purity, concurrence, tangle, entanglement of formation, and possibly Bell state fidelity are computed. We then have an insight into the statistical distributions of the entanglement measure values for the measured state.

true value of the projection. What follows immediately from this is the notion that upon repeating the tomographical procedure, we would also observe fluctuations in the density matrix estimates, and the resulting entanglement measures. The task that lies in front of us then is to assess the statistical distribution of the density matrix and entanglement measure estimates, and to obtain confidence intervals, especially for the values of entanglement measures.

One method of achieving this is repeated measurement. This approach is obviously very time-consuming, and applying it to all the presented data sets is not feasible. This can be circumvented, however, by a Monte Carlo simulation. If we consider the coincidence counts $\{n_i\}_{i=1}^{36}$ for the 36 projection measurements to be random variables with Poissonian distributions

$$\{P_i(n)\}_{i=1}^{36}, \qquad P_i(n) = \frac{\mathrm{e}^{-\lambda_i}\lambda_i^n}{n!}, \tag{3.22}$$

where we identify the means λ_i of the distributions with the measured coincidence counts, we can programatically sample the coincidence count values according to these distributions, perform the MaxLik density matrix estimation algorithm, and evaluate the entanglement measures, as shown in Figure 3.6. Finally, we can study the statistical distribution of the resulting data, which will lead us to the confidence intervals.

When we present the results of the Monte Carlo sampling of entanglement measures, we will limit ourselves to the mean value and the standard deviation only. This is common for many estimates. It should be noted, however, that the results will most likely not obey the Gaussian distribution, and might in fact have more complicated statistics. Then the mean and the standard deviation do not give us all the information about the statistical distribution of the entanglement measure value estimates. In principle, this might be a cause for concern to a skeptic, as any outlying values would go unnoticed. The presence of outliers very far below the mean would imply that while taking into account the Poissonian statistics of the coincidence counts collected during a measurement, there might be a chance that the measured state might not be as well entangled as the mean value of the

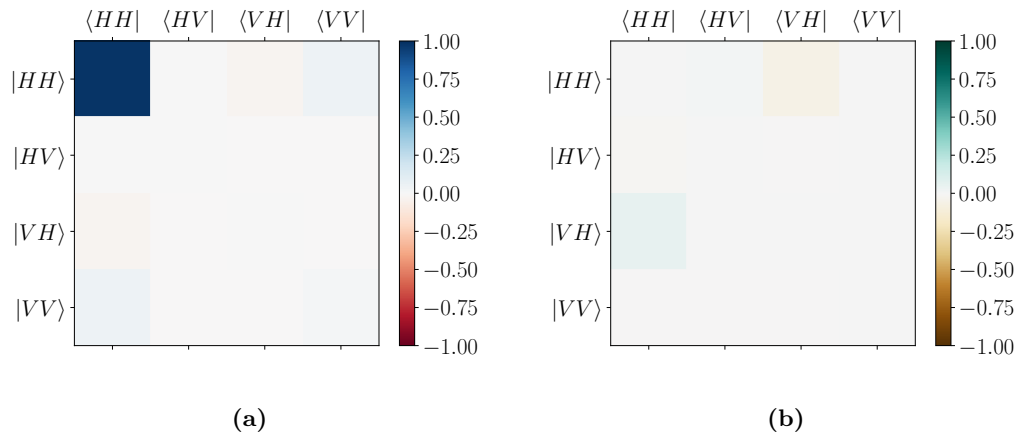

Figure 3.7: Test of the quantum state estimation procedure. The real (a) and imaginary (b) parts of the density matrix of the $|HH\rangle$ state generated by the SPDC source are shown. The purity of the state is $\gamma = 0.969(2)$.

entanglement measure estimates would suggest. In an attempt to counter this argument, we will later present the shape of the distributions of the entanglement measures for one case of Monte Carlo error propagation. We will see that, albeit not Gaussian, the distributions contain no outlying values. We will then make the assumption that the statistics of all other Monte Carlo samplings are similar to the one presented, and carry on using the mean and standard deviation for the characterization of the results.

3.7 Tomography of the pairs generated without compensations

To demonstrate proper functionality of the tomography scheme and the quantum state estimation, we perform the tomographical procedure on an example state $|HH\rangle$. To generate such a state using the SPDC source, a HWP placed before the crystal is adjusted so that the pump beam is vertically polarized when incident on the BiBO crystals. One of the two crystals then generates pairs of horizontally polarized photons, as dictated by the Type-I phase matching.

The mechanical stresses inside the optical fibers causes the polarizations of the signal and idler photons to undergo unknown unitary transformations $U_\mathrm{s}, U_\mathrm{i}$. To mitigate this, the HWPs and QWPs used in the tomography scheme are set to angles corresponding to the $|HH\rangle$ projection, and fiber polarization controllers (PCs) are adjusted until the coincidence rate is maximized for both signal and idler. When this is accomplished, the PCs introduce additional mechanical stress into the fibers, which further transforms the state of signal and idler by $U_\mathrm{s}^\dagger$ and $U_\mathrm{i}^\dagger$, respectively. Combined with the previous unitary transforms, the polarization states of signal and idler after the fibers are identical as before the fibers, except for a global phase factor.

With correctly compensated fiber unitary transforms, the tomographical routine can proceed. We use a coincidence window of approximately 7 ns, and count coincidences for one second per projection. Polarization projections are measured in the TSP-optimized order, and the resulting coincidence counts are fed into the MaxLik algorithm. The estimated density matrix is shown in Figure 3.7. The values of the entanglement measures are of no interest to us at this point, hence we only evaluate the purity of the state, which is estimated using the Monte Carlo sampling to be $\gamma = 0.969(2)$.

Finally, we proceed to estimate and characterize the output state of the SPDC entanglement source,

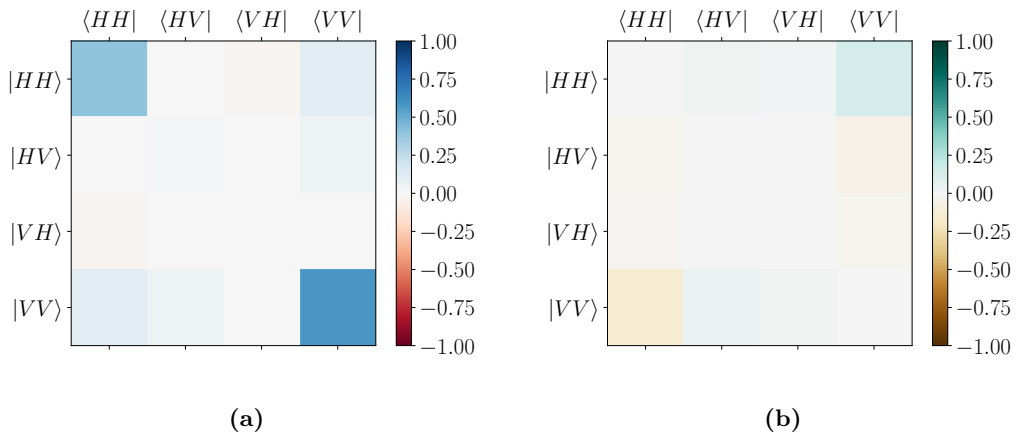

Figure 3.8: The real (a) and imaginary (b) parts of the density matrix of the photon pair state generated by the SPDC source with diagonally polarized input beam. No compensating elements were present at this stage. Purity: $\gamma = 0.573(3)$, concurrence: $C = 0.347(6)$, tangle: $T = 0.120(4)$, entanglement of formation: $E = 0.200(5)$.

without any compensating elements present. Before this and every measurement that will follow, proper cancellation of the fiber-induced unitary transforms $U_\mathrm{s}, U_\mathrm{i}$ must be ensured. This means pumping the SPDC crystals vertically, generating the HH state, and adjusting the PCs to maximize the coincidence rate for the HH state projection. We arrive at a coincidence rate of approximately 16,000 per second. With roughly 90,000 detector clicks per second for both signal and idler, our two-photon coupling efficiency is then

$$\eta \approx \frac{16000}{\sqrt{90000 \times 90000}} \approx 17.8\,\%. \tag{3.23}$$

When successful elimination of the fiber-induced unitary transformation is accomplished, the HWP before the crystals is rotated so that the pump beam is polarized diagonally. The tomographical procedure can then start. The resulting density matrix estimate is shown in Figure 3.8. We can see that the desired off-diagonal elements $|HH\rangle\langle VV|$ and $|VV\rangle\langle HH|$ are present but rather small. The values of the entanglement measures, summarized in the caption of Figure 3.8 show that some entanglement is present. The evaluation of the PPT criterion supports this. With concurrence $C = 0.347(6)$, however, we are far from the highly entangled state we ultimately seek.

4 Compensations

4.1 The reason behind entanglement degradation

The bipartite state generated by the SPDC photon pair source so far is not perfectly entangled. To explain this, imagine that the source is set up to generate—in the ideal scenario—the following Bell state:

$$|\Psi_{\text{ideal}}\rangle = |HH\rangle + |VV\rangle \tag{4.1}$$

What happens in the real case is that Bell states with various phases δ

$$|\Psi(\delta)\rangle = |HH\rangle + \mathrm{e}^{i\delta}|VV\rangle \tag{4.2}$$

are generated, and the state that we measure is in fact a mixture of these states $|\Psi(\delta)\rangle$:

$$\rho_{\text{real}} = \int_0^{2\pi} C(\delta)\,|\Psi(\delta)\rangle\langle\Psi(\delta)|\,\mathrm{d}\delta \tag{4.3}$$

where $C(\delta)$ is a weight function normalized to unity. Depending on the shape of $C(\delta)$, the entanglement of the real state ρ_{real} can be more or less deteriorated. To eliminate this undesirable outcome, compensating techniques are required in order to flatten the profile of the phase δ across the regions in space and time where we collect the signal and idler photons.

An alternative explanation for entanglement degradation in the measured state is the presence of *which-crystal information*. In the same scenario as above, we would ideally be generating the Bell state from Equation (4.1). Therefore, in both the signal and the idler arms of the setup, we would encounter photons from both of the two SPDC crystals. If we were, even in principle only, able to tell which one of the two crystals had a given photon been generated in, we would reduce the quality of entanglement in the generated photon pair. While adopting this point of view, we can identify two major causes of entanglement deterioration, caused by the birefringence of the SPDC crystals. They are called the *spatial* and *temporal walk-off*.

Spatial walk-off occurs in birefringent media and is caused by the fact that the Poynting vector, which signifies the direction of energy flow, is not in general collinear with the direction of propagation in the media. In practice, this means that the signal and idler beams generated in the two SPDC crystals are each differently distorted and that $C(\delta)$ has a non-trivial spatial profile. In our case of Type-I phase matched SPDC entanglement source, compensating walk-off means making sure that it is, not even in principle, possible to tell from the spatial profile of the outcoming beams the photons generated in one crystal from the photons generated in the other one. This is done using *post-compensators*—birefringent crystals placed in the signal and idler arms of the entanglement source geometry [35, 60]. If oriented correctly, these crystals effectively make sure that the spatial profiles of the photons from both crystals match as closely as possible.

We make use of a two-crystal scheme for entanglement generation. As the pump reaches one of the crystals sooner than the other, the generated photons are slightly displaced in time. This temporal displacement, or *temporal walk-off* is a source of which-crystal information, and ultimately leads to entanglement degradation. Compensation of temporal walk-off is achieved by placing a birefringent *pre-compensator* before the two SPDC crystals [35, 60]. If the pre-compensator is oriented so that

the polarization component of the pump that reaches the first SPDC crystal is delayed by the right amount of time, the temporal walk-off is successfully eliminated. This technique can be used even if the pump is very broad-band, as is the case for pulse lasers [34, 35].

4.2 The effect of compensations

After a discussion of walk-off of both kinds, and the respective compensation techniques, we proceed to study their effect on the quality of entanglement in the photon pairs generated by our entanglement source. First, we insert a post-compensator in the signal arm of the setup. We change the angle φ_s of the optical axis of the post-compensator from 0 ° to 180 °, with 22.5 ° steps, and perform a full quantum state tomography and Monte Carlo estimation of the entanglement measures every time. In Figure 4.1 we present the observed dependence of the quantum state concurrence on the orientation of the pre-compensator. We find a maximum concurrence of $C = 0.362(9)$ for $\varphi_s = 180$ °.

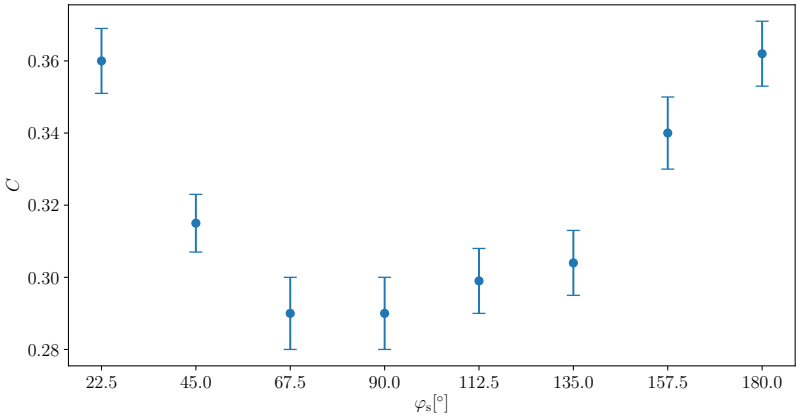

Figure 4.1: The dependence of concurrence on the orientation of the post-compensating crystal in the signal arm of the entanglement source geometry. No other compensating elements were present. The angle φ_s is taken with respect to the optical axis of the crystal. The highest observed concurrence $C = 0.362(9)$ was achieved for $\varphi_s = 180$ °. The error bars correspond to the standard deviation of the Monte-Carlo-sampled concurrence.

This concurrence-maximizing procedure has been repeated as the other compensating elements were added to the setup. The orientation of the signal post-compensator was fixed at φ_s and a post-compensator for idler was placed, and concurrence maximized again. The effect on the concurrence of the produced quantum state was not great, and the maximal concurrence ever observed with only the post-compensators in place was $C \approx 0.41$. We believe that the reason for the low gain in concurrence lies in the fact that our entanglement source is fiber-coupled, and that the spatial filtering performed inherently by the process of coupling into fiber did good enough job to mitigate spatial walk-off, allowing us to observe some, albeit low-quality, entanglement event without the post-compensators.

Finally, the pre-compensator was placed and the maximization was performed once over. We observed a significant increase in the concurrence of the produced quantum state. What followed was another round of concurrence maximization. This time, however, the angular orientations of all the compensating elements were kept fixed, and the only two degrees of freedom were the horizontal and vertical tilt of the pre-compensator. Using this method, we were able to generate the quantum state

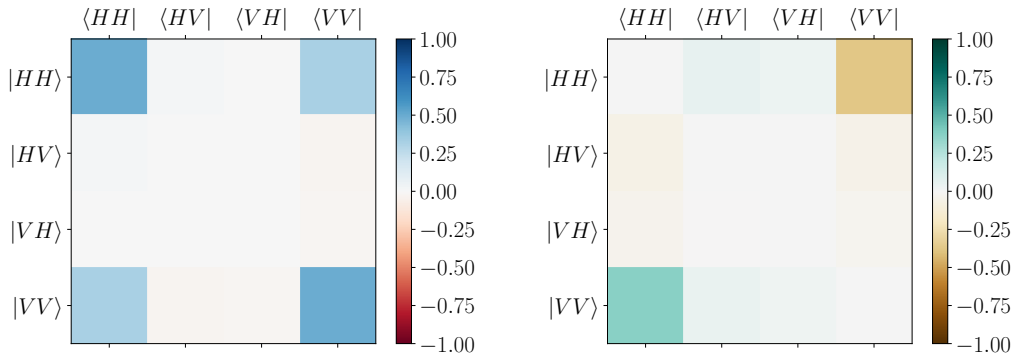

(a) **(b)**

Figure 4.2: Real (a) and imaginary (b) parts of the density matrix of the SPDC entanglement source output with all compensating elements present. Purity: $\gamma = 0.988(4)$, concurrence: $C = 0.988(4)$, tangle: $T = 0.976(8)$, entanglement of formation: $E = 0.982(6)$, Bell state fidelity: $\mathcal{F}^{(\psi_B)} = 0.984(2)$.

represented by the density matrix shown in Figure 4.2. We arrived at $C = 0.988(4)$, which has so far been our best result. The Bell state fidelity (3.21) has also been evaluated for this quantum state, the target Bell state being $|\psi_B\rangle = \frac{1}{\sqrt{2}}(|HH\rangle + |VV\rangle)$. The off-diagonal elements of the estimated density matrix are not purely real. We hypothesize that this is due to the presence of mirror $\mathtt{M_p}$ after the half-wave plate $\mathtt{HWP_p}$ that controls the polarization of the pump beam. We attribute the undesired transformation of our density matrices to the fact that the diagonal polarization of light incident on the mirror is distorted as it is reflected. We plan to test this hypothesis, and to eliminate the unwanted transformation, by swapping the order of $\mathtt{M_p}$ and $\mathtt{HWP_p}$. For now, however, the density matrix has been transformed by a unitary transformation

$$\tilde{\rho} \equiv \tilde{U}\rho\,\tilde{U}^\dagger, \qquad \tilde{U} = \begin{pmatrix} 1 & 0 \\ 0 & 1 \end{pmatrix} \otimes \begin{pmatrix} 1 & 0 \\ 0 & \mathrm{e}^{i\delta} \end{pmatrix} \tag{4.4}$$

with δ chosen to maximize $\mathcal{F}^{(\rho_B)}$. The resulting fidelity is $\mathcal{F}^{(\rho_B)} = 0.984(2)$. The values of the other entanglement measures are stated in the caption of Figure 4.2.

Furthermore, at this point we fulfill the promise given in Chapter 3, and present more details of the statistical distributions of the Monte-Carlo-sampled values of the entanglement measures. The violin plots in Figure 4.3 show the probability distributions of each of the five quantifiers we use to characterize our photon pair states. It can be seen that there are no outliers. This means that there is no room for doubts about the high quality of entanglement in the state we produced.

In the regime presented above, with narrow-band interference filters in the signal and idler arms of the experiment, we observe roughly 16,000 coincidences per second. This value was obtained by pumping the BiBO crystals vertically, and measuring the HH state projection. With the goal of achieving even greater pair generation rate, we temporarily replaced the interference filters with a broader-band (10 nm) filters. The coincidence rate then climbed to almost 100,000/s. In this regime, we performed again the full quantum state tomography and estimation of the entanglement measures. We arrived at $\gamma = 0.962(2)$, $C = 0.962(2)$, $T = 0.926(3)$, $E = 0.946(2)$, and, with the help of a unitary transform, $\mathcal{F}^{(\rho_B)} = 0.9676(8)$. We are certain that with some adjustments to the rotation and tilt of the compensating elements, even better values could be obtained. These results give our entanglement source the possibility of operation in two regimes. If extremely high quality of entanglement is desired,

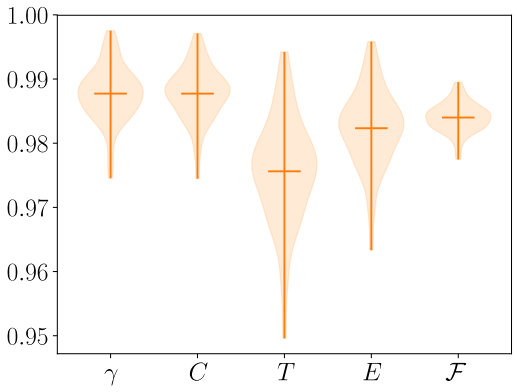

Figure 4.3: The statistical distributions of the values of entanglement measures obtained using the Monte Carlo sampling method. γ: purity, C: concurrence, T: tangle, E: entanglement of formation, $\mathcal{F}$: Bell state fidelity.

the narrow-band filters can be used. If, on the other hand, we seek higher pair generation rate, and are willing to make a little sacrifice in terms of entanglement quality, the 10 nm filters can be used instead.

5 Conclusions and outlook

The presented experimental realization of an SPDC-based source of entangled photon pairs is on par with similar setups [34, 35]. By employing compensating elements, we were able to produce bipartite quantum states with a high concurrence $C \approx 0.99$. This was achieved using narrow-band interference filters in the signal and idler arms of the experiment, limiting the coincidence count rate to approximately $16\,000\,\mathrm{s}^{-1}$. By replacing these filters with wider, 10 nm filters, the coincidence count climbed to almost $100\,000\,\mathrm{s}^{-1}$, while the concurrence was still high, with a value of $C \approx 0.96$. This makes the setup ready for use in further experimental applications.

We studied in detail the tomographical procedure, and found that it can be considerably sped up if an optimal order of polarization projection measurements is chosen. Apart from optimizing our quite specific scenario, with one faster and three slower rotation mounts, and reaching a speedup factor of 1.71, we solved the tomographical TSPs for systems of increasing complexity, stopping at a five-qubit system. Relying on angular specification required only the easily satisfied condition that all mounts used rotate equally fast, and made the results hardware-independent. The speedup factor we found increases with the size of the system, and is available to all of the many experiments that rely on characterization of quantum states or processes. A nice feature of the speedup achieved using TSP optimization is that no changes need to be made to existing experimental setups hardware-wise. It is only the order of polarization projection measurements that is shuffled.

One of the changes the experimental setup might undergo in the future is switching from a continual pump to a pulsed one. The source has been designed with this in mind, and the angularly-tuned scheme should allow an easy transition. Furthermore, the position of the half-wave plate $\mathrm{HWP_p}$ (see Figure 2.3) that controls the polarization of the pump might be changed, so that the diagonal polarization of the pump is not distorted by the mirror $\mathrm{M_p}$. We believe that this will enable our source to generate Bell states unburdened by an undesired unitary transformation unlike the state in Figure 4.2.

Being able to generate any of the four Bell states on demand would be a welcome additional feature of the entanglement source. In the original Type-I phase matched source [28], this was achieved using a QWP in front of the pair of SPDC crystals. Tilting the QWP changed the phase of the superposition state. Additionally, by introducing a single HWP in either the signal or idler arms of the geometry, we would be readily able to swap horizontal and vertical polarization in the said arm, allowing the transition between the states $\frac{1}{\sqrt{2}}\left(|HH\rangle + \mathrm{e}^{i\delta}|VV\rangle\right)$ and $\frac{1}{\sqrt{2}}\left(|HV\rangle + \mathrm{e}^{i\delta}|VH\rangle\right)$.

If it was necessary to reduce the duration of the quantum state tomography even further, it would be possible to use a minimal set of projections. This would lead to 14 measurements instead of 36. We expect that the total duration of the procedure would by reduced by nearly 50%. Lastly, we could replace the waveplate-based tomography scheme and use liquid crystal (LC) modules, instead [61]. The switching between various configurations of the LCs is very fast compared to the rotating mounts, and a great reduction in total tomography time would follow. The real bottleneck would then be the counting time required for each projection measurement.

Finally, it might be desirable in the future to measure additional characteristics of the generated quantum state. To benchmark the indistinguishability of the two photons generated in each pair, the visibility of the Hong-Ou-Mandel interference [62] might be measured. To further characterize entanglement, a measurement of the Bell inequalities [2, 3] might be performed.

Bibliography

[1] A. Einstein, B. Podolsky, and N. Rosen, "Can quantum-mechanical description of physical reality be considered complete?," *Phys. Rev.*, vol. 47, p. 777, 1935.

[2] J. S. Bell, "On the Einstein Podolsky Rosen paradox," *Physics*, vol. 390, p. 575, 1964.

[3] J. F. Clauser, M. A. Horne, A. Shimony, and R. A. Holt, "Proposed experiment to test local hidden-variable theories," *Physical Review Letters*, vol. 23, no. 15, p. 880, 1969.

[4] S. J. Freedman and J. F. Clauser, "Experimental test of local hidden-variable theories," *Phys. Rev. Lett.*, vol. 28, no. 14, pp. 938–, 1972.

[5] A. Aspect, P. Grangier, and G. Roger, "Experimental realization of Einstein-Podolsky-Rosen-Bohm gedankenexperiment: A new violation of Bell's inequalities," *Phys. Rev. Lett.*, vol. 49, no. 2, p. 91, 1982.

[6] B. Hensen, H. Bernien, A. E. Dréau, A. Reiserer, N. Kalb, M. S. Blok, J. Ruitenberg, R. F. L. Vermeulen, R. N. Schouten, C. Abellán, W. Amaya, V. Pruneri, M. Mitchell, M. Markham, D. J. Twitchen, D. Elkouss, S. Wehner, T. H. Taminiau, and R. Hanson, "Loophole-free Bell inequality violation using electron spins separated by 1.3 kilometres," *Nature*, vol. 526, p. 682, 2015.

[7] M. Giustina, M. A. M. Versteegh, S. Wengerowsky, J. Handsteiner, A. Hochrainer, K. Phelan, F. Steinlechner, J. Kofler, J.-A. Larsson, C. Abellán, W. Amaya, V. Pruneri, M. W. Mitchell, J. Beyer, T. Gerrits, A. E. Lita, L. K. Shalm, S. W. Nam, T. Scheidl, R. Ursin, B. Wittmann, and A. Zeilinger, "Significant-loophole-free test of Bell's theorem with entangled photons," *Phys. Rev. Lett.*, vol. 115, p. 250401, 2015.

[8] G. Brassard and A. A. Méthot, "Can quantum-mechanical description of physical reality be considered incomplete?," *Int. J. Quantum Inform.*, vol. 04, 2006.

[9] C. H. Bennett, G. Brassard, C. Crépeau, R. Jozsa, A. Peres, and W. K. Wooters, "Teleporting an unknown quantum state via dual classical and Einstein-Podolsky-Rosen channels," *Phys. Rev. Lett.*, vol. 70, no. 13, p. 1895, 1993.

[10] D. Bouwmeester, J.-W. Pan, K. Mattle, M. Eibl, H. Weinfurter, and A. Zeilinger, "Experimental quantum teleportation," *Nature*, vol. 390, p. 575, 1997.

[11] H. Paul, *Introduction to Quantum Optics: From Light Quanta to Quantum Teleportation*. Cambridge University Press, 2004.

[12] C. H. Bennett and G. Brassard, "Quantum cryptography: Public key distribution and coin tossing," in *International Conference on Computers, Systems & Signal Processing*, 1984.

[13] C. H. Bennett, F. Bessette, G. Brassard, L. Salvail, and J. Smolin, "Experimental quantum cryptography," *Journal of Cryptology*, vol. 5, no. 1, p. 3, 1992.

[14] C. H. Bennett, "Quantum cryptography using any two nonorthogonal states," *Phys. Rev. Lett.*, vol. 68, p. 3121, 1992.

[15] A. Muller, J. Breguet, and N. Gisin, "Experimental demonstration of quantum cryptography using polarized photons in optical fibre over more than 1 km," *Europhys. Lett.*, 1993.

[16] A. K. Ekert, "Quantum cryptography based on Bell's theorem," *Phys. Rev. Lett.*, vol. 67, no. 6, p. 661, 1991.

[17] A. K. Ekert, J. G. Rarity, P. R. Tapster, and G. M. Palma, "Practical quantum cryptography based on two-photon interferometry," *Phys. Rev. Lett.*, vol. 69, p. 1293, 1992.

[18] W. Diffie and M. Hellman, "New directions in cryptography," *IEEE Transactions on Information Theory*, vol. 22, p. 644, 1976.

[19] R. L. Rivest, A. Shamir, and L. Adleman, "A method for obtaining digital signatures and public-key cryptosystems," *Communications of the ACM*, vol. 21, p. 120, 1978.

[20] P. W. Shor, "Polynomial-time algorithms for prime factorization and discrete logarithms on a quantum computer," *SIAM Review*, vol. 41, no. 2, p. 303, 1999.

[21] V. M. Kendon and J. W. Munro, "Entanglement and its role in Shor's algorithm," *Quantum Info. Comput.*, vol. 6, no. 7, p. 630, 2006.

[22] I. M. Georgescu, S. Ashhab, and F. Nori, "Quantum simulation," *Rev. Mod. Phys.*, vol. 86, p. 153, 2014.

[23] R. Islam, C. Senko, W. C. Campbell, S. Korenblit, J. Smith, A. Lee, E. E. Edwards, C.-C. J. Wang, J. K. Freericks, and C. Monroe, "Emergence and frustration of magnetism with variable-range interactions in a quantum simulator," *Science*, vol. 340, p. 583, 2013.

[24] H. Bernien, S. Schwartz, A. Keesling, H. Levine, A. Omran, H. Pichler, S. Choi, A. S. Zibrov, M. Endres, M. Greiner, V. Vuletić, and M. D. Lukin, "Probing many-body dynamics on a 51-atom quantum simulator," *Nature*, vol. 551, p. 579, 2017.

[25] N. Friis, O. Marty, C. Maier, C. Hempel, M. Holzäpfel, P. Jurcevic, M. B. Plenio, M. Huber, C. Roos, R. Blatt, and B. Lanyon, "Observation of entangled states of a fully controlled 20-qubit system," *Phys. Rev. X*, vol. 8, p. 021012, 2018.

[26] H. Labuhn, D. Barredo, S. Ravets, S. de Léséleuc, T. Macrì, T. Lahaye, and A. Browaeys, "Tunable two-dimensional arrays of single Rydberg atoms for realizing quantum ising models," *Nature*, vol. 534, p. 667, 2016.

[27] P. G. Kwiat, K. Mattle, H. Weinfurter, and A. Zeilinger, "New high-intensity source of polarization-entangled photon pairs," *Phys. Rev. Lett.*, vol. 75, no. 24, p. 4337, 1995.

[28] P. G. Kwiat, E. Waks, A. G. White, I. Appelbaum, and P. H. Eberhard, "Ultrabright source of polarization-entangled photons," *Phys. Rev. A*, vol. 60, no. 2, p. R773, 1999.

[29] T. Chanelière, D. N. Matsukevich, S. D. Jenkins, T. A. B. Kennedy, M. S. Chapman, and A. Kuzmich, "Quantum telecommunication based on atomic cascade transitions," *Phys. Rev. Lett.*, vol. 96, p. 093604, 2006.

[30] R. T. Willis, F. E. Becerra, L. A. Orozco, and S. L. Rolston, "Photon statistics and polarization correlations at telecommunications wavelengths from a warm atomic ensemble," *Opt. Express*, vol. 19, no. 15, p. 14632, 2011.

[31] Z. Zheng, H. Wang, B. Cheng, and J. Jing, "Entanglement in a four-wave mixing process," *Opt. Lett.*, vol. 42, no. 14, p. 2754, 2017.

[32] W. P. Risk and S. D. Lau, "Periodic electric field poling of $KTiOPO_4$ using chemical patterning," *Appl. Phys. Lett.*, vol. 69, p. 3999, 1996.

[33] G. W. Ross, M. Pollnau, P. G. R. Smith, W. A. Clarkson, P. E. Britton, and D. C. Hanna, "Generation of high-power blue light in periodically poled $LiNbO_3$," *Opt. Lett.*, vol. 23, no. 3, p. 171, 1998.

[34] Y. Nambu, K. Usami, Y. Tsuda, K. Matsumoto, and K. Nakamura, "Generation of polarization-entangled photon pairs in a cascade of two type-I crystals pumped by femtosecond pulses," *Phys. Rev. A*, vol. 66, p. 033816, 2002.

[35] R. Rangarajan, M. Goggin, and P. Kwiat, "Optimizing type-I polarization-entangled photons," *Opt. Express*, vol. 17, no. 21, p. 18920, 2009.

[36] J. E. Sharping, M. Fiorentino, A. Coker, P. Kumar, and R. S. Windeler, "Four-wave mixing in microstructure fiber," *Opt. Lett.*, vol. 26, no. 14, p. 1048, 2001.

[37] J. Chen, X. Li, and P. Kumar, "Two-photon-state generation via four-wave mixing in optical fibers," *Phys. Rev. A*, vol. 72, p. 033801, 2005.

[38] X. Li, P. L. Voss, J. E. Sharping, and P. Kumar, "Optical-fiber source of polarization-entangled photons in the 1550 nm telecom band," *Phys. Rev. Lett.*, vol. 94, p. 053601, 2005.

[39] E. Y. Zhu, Z. Tang, L. Qian, L. G. Helt, M. Liscidini, J. E. Sipe, C. Corbari, A. Canagasabey, M. Ibsen, and P. G. Kazansky, "Direct generation of polarization-entangled photon pairs in a poled fiber," *Phys. Rev. Lett.*, vol. 108, p. 213902, 2012.

[40] E. Y. Zhu, Z. Tang, L. Qian, L. G. Helt, M. Liscidini, J. E. Sipe, C. Corbari, A. Canagasabey, M. Ibsen, and P. G. Kazansky, "Poled-fiber source of broadband polarization-entangled photon pairs," *Opt. Lett.*, vol. 38, no. 21, p. 4397, 2013.

[41] R. W. Boyd, *Nonlinear Optics*. Elsevier LTD, Oxford, 2008.

[42] M. A. M. Versteegh, M. E. Reimer, K. D. Jöns, D. Dalacu, P. J. Poole, A. Gulinatti, A. Giudice, and V. Zwiller, "Observation of strongly entangled photon pairs from a nanowire quantum dot," *Nature Communications*, vol. 5, p. 5298, 2014.

[43] J. Zhang, Y. Huo, A. Rastelli, M. Zopf, B. Höfer, Y. Chen, F. Ding, and O. G. Schmidt, "Single photons on-demand from light-hole excitons in strain-engineered quantum dots," *Nano Lett.*, vol. 15, no. 1, p. 422, 2015.

[44] D. D. B. Rao, S. Yang, and J. Wrachtrup, "Generation of entangled photon strings using NV centers in diamond," *Phys. Rev. B*, vol. 92, p. 081301, 2015.

[45] A. Cavanna, F. Just, X. Jiang, G. Leuchs, M. V. Chekhova, P. S. Russell, and N. Y. Joly, "Hybrid photonic-crystal fiber for single-mode phase matched generation of third harmonic and photon triplets," *Optica*, vol. 3, no. 9, p. 952, 2016.

[46] P. J. Shadbolt, M. R. Verde, A. Peruzzo, A. Politi, A. Laing, M. Lobino, J. C. F. Matthews, M. G. Thompson, and J. L. O'Brien, "Generating, manipulating and measuring entanglement and mixture with a reconfigurable photonic circuit," *Nature Photonics*, vol. 6, p. 45, 2012.

[47] I. Straka, "Optical frequency conversion and non-classical light generation," Master's thesis, Palacky University, 2012.

[48] J. Bílek, "Jednofotonové zdroje a jejich prostorové vlastnosti," Master's thesis, Palacky University, 2015.

[49] H. Hellwig, J. Liebertz, and L. Bohatý, "Linear optical properties of the monoclinic bismuth borate BiB_3O_6," *J Appl Phys*, vol. 88, no. 1, p. 240, 2000.

[50] M. Ebrahim-Zadeh, "BiB_3O_6 offers competitive edge over recognized rivals," *SPIE Newsroom*, 2007.

[51] D. F. V. James, P. G. Kwiat, W. J. Munro, and A. G. White, "Measurement of qubits," *Phys. Rev. A*, vol. 64, p. 052312, 2001.

[52] E. L. Lawler, J. K. Lenstra, A. H. G. R. Kan, and D. B. Shmoys, *The Traveling Salesman Problem*. John Wiley and Sons, 1985.

[53] "Concorde TSP." `http://www.math.uwaterloo.ca/tsp/concorde.html`. Accessed: 2017-10-20.

[54] R. Hošák, R. Stárek, and M. Ježek, "The optimal strategy for photonic multi-qubit quantum tomography," 2018. In preparation.

[55] R. Hošák, "tomo-tsp." `https://github.com/rhosak/tomo-tsp`, 2018.

[56] G. Reinelt, "TSPLIB—a traveling salesman problem library," *INFORMS J Comput*, vol. 3, p. 376, 1991.

[57] Z. Hradil, "Quantum-state estimation," *Phys. Rev. A*, vol. 55, p. R1561, 1997.

[58] M. Paris and J. Řeháček, *Quantum State Estimation*. Springer, 2004.

[59] J. Řeháček, Z. Hradil, and M. Ježek, "Iterative algorithm for reconstruction of entangled states," *Phys. Rev. A*, vol. 63, p. 040303, 2001.

[60] A. Cavanna, A. M. Pérez, F. Just, M. V. Chekhova, and G. Leuchs, "Compensation of anisotropy effects in the generation of two-photon light," *Opt. Express*, vol. 22, no. 8, p. 9983, 2014.

[61] M. Bielak, "Electro-optic control of photonic quantum bits." Bachelor's Thesis, Palacky University, 2017.

[62] C. K. Hong, Z. Y. Ou, and L. Mandel, "Measurement of subpicosecond time intervals between two photons by interference," *Phys. Rev. Lett.*, vol. 59, no. 18, p. 2044, 1987.